Cross-sectional shape optimization of whispering-gallery ring resonators

Akihiro Takezawa, Mitsuru Kitamura

***Abstract*—Optimal cross-sectional shapes of whispering-gallery ring resonators with prescribed emission wavelength and resonance mode are generated using topology optimization based on the finite element method. The two critical performance indices, the quality factor (Q factor) and mode volume of a resonator, are treated as the objective functions in the optimization. In our numerical study, characteristics of optimal configurations are identified and analyzed. Since the Q factor and mode volume have a trade-off relationship, *i.e.*, an increasing Q factor increases mode volume, a Pareto-optimal set of solutions can be identified under certain device specifications. These configurations achieve better performances than existing shapes in producing both a high Q factor and low mode volume.**

I. Introduction

Micro-ring resonators have tremendous potential in optics with applications to low threshold microcavity lasers and light-matter systems for quantum networking [1], [2], [3], [4]. The optical modes, set up in these devices by emissions from input light, form circular continuous closed beams governed by internal reflections along the boundary of the resonator. The circular mode shape is called a whispering-gallery (WG) mode. Optical resonators exploiting WG modes have been attaining high levels in the important typical-performance criteria for resonators, *i.e.*, high quality factor (Q factor) which measures the inverse of the decay rate of the energy and low mode volume which signifies the spatial confinement of the light [5]. In other words, the light wave is trapped within a very small volume during WG mode emission.

Both performance criteria depend on emission wavelength, refraction index of the material, and device shape. In designing novel devices with existing dielectric materials under a specified emission wavelength, device shape must be paramount. The search for novel device geometry can be assisted by accurate numerical performance analysis using the finite-element method (FEM). In particular, due to the circular shape of the device and the optical mode, axisymmetric models are effective at simulating the WG resonance mode in ring resonators. Details are explained in [6]. Using FEM, simple geometric parametric studies have been performed for disc shapes [7] and toroidal shapes [8]. Rough relationships between geometry, WG mode order and performance indices were established, such that the larger radius of the device yields larger Q factor and high mode volume. However, a detailed search for an ideal device shape remains an open problem. Moreover, since varying the device shape varies the resulting WG mode order and emission wavelength, a detailed search for an optimal shape is quite challenging for a specified wavelength. Thus, integrating existing parametrical studies and detailed shape optimization provides a means to develop high performance devices that would be available for a wide variety of uses.

Topology optimization [9] has contributed to optimal designs in novel wave propagation devices in photonics [10], [11], [12], [13], [14], [15]. In the approach, the designed devices are represented as distributions of the dielectric material or metal in the analysis model. By updating the distribution by the gradient-based optimization method, the generated distribution represents the shape of devices that attain specific performance criteria.

In this research, we study and identify optimal shapes for WG micro-ring resonators using FEM-based topology optimization. The systematic procedure helps to find optimal device shapes with fixed design performance given a prescribed emission wavelength and WG resonance mode. The analysis domains and the equations of state for the WG mode ring resonators are first considered. The Q factor, mode volume, and emission wavelength are formulated as objective functions and an equality constraint. The proposed geometrical optimization is implemented as a distribution optimization of the dielectric material using the solid isotropic material with the penalization (SIMP) method of topology optimization [9]. The optimization algorithm is constructed based on the two-times FEM analysis, sensitivity analysis for each objective function and density function constraint, and sequential linear programming (SLP) with a phase field method [16]. Finally, numerical examples are provided as a validation of the proposed methodology. As a compromise is required between the two important performance indices, Q factor and mode volume, *i.e.* increasing the Q factor increases the mode volume, a Pareto-optimal set of solutions [17] can be identified once given device specifications. Optimization maximizing Purcell factor [18], a practical design parameter for resonators, is also performed.

II. Problem settings

A. Analysis model

Using cylindrical coordinates, we model a WG ring resonator centered on the origin in free space as illustrated in Fig. 1. The coordinate system composed of components (z, ϕ, r) are the axial, azimuthal, and radial coordinates respectively. The vertical cross-sectional shape of the device in the z-r plane, is treated as the design target; we obtain the final

A. Takezawa and M. Kitamura are with the Division of Mechanical System and Applied Mechanics, Faculty of Engineering, Hiroshima University, Higashi-Hiroshima, Hiroshima 739-8527, Japan e-mail: akihiro@hiroshima-u.ac.jp.

axisymmetric form by generating the solid of revolution. The domain is enclosed by a so-called perfect matched layer (PML) domain.

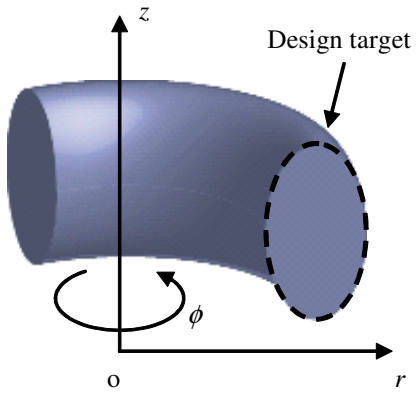

Fig. 1. The analysis and design domain as described by cylindrical coordinates

B. Equations of state

The equations of state representing resonance-mode wave propagation within the domain are the 3D vector Helmholtz equations. If the resonator medium is isotropic, the Helmholtz equation for the magnetic field $\boldsymbol{H}$, as derived from Maxwell's equation, is written as follows:

$$\nabla \times \left(\frac{1}{\epsilon}\nabla \times \boldsymbol{H}\right) - \frac{1}{c^2}\frac{\partial^2 \boldsymbol{H}}{\partial t^2} = 0 \tag{1}$$

where ϵ is the relative permittivity and c the speed of light. Here, the time harmonic function is assumed in the form $\boldsymbol{H}(\boldsymbol{x},t) = \boldsymbol{H}(\boldsymbol{x})e^{i\omega t}$ and the above equation is solved as an eigenvalue problem by FEM, where $\omega = 2\pi f$ is the angular resonance frequency given resonance frequency f. To suppress spurious modes in the analysis, a weak penalty term [19] is introduced to yield the following modified equation used in [6]:

$$\nabla \times \left(\frac{1}{\epsilon}\nabla \times \boldsymbol{H}\right) - \alpha\nabla\left(\nabla \cdot \boldsymbol{H}\right) + \frac{\omega^2}{c^2}\boldsymbol{H} = 0 \tag{2}$$

where α is a coefficient. The following two types of boundary conditions for the above equation are considered:

$$\boldsymbol{H} \times \hat{\boldsymbol{n}} = 0 \text{ on } \Gamma_{\text{pmc}} \tag{3}$$

$$\hat{\boldsymbol{n}} \times \nabla \times \boldsymbol{H} + ik\hat{\boldsymbol{n}} \times \hat{\boldsymbol{n}} \times \boldsymbol{H} = 0 \text{ on } \Gamma_{\text{abc}} \tag{4}$$

where k is the wave number in free-space and $\hat{\boldsymbol{n}}$ is the unit vector normal to the boundary; the former describing perfect magnetic conduction and the latter first-order absorption on the boundary.

The state variable is the set comprising the time-dependent radial, azimuthal, and axial components of the magnetic field vector $\boldsymbol{H}(\boldsymbol{r},t)$. We factorize the azimuthal-dependence from the variable using the cylindrical coordinate system; that is,

$$\boldsymbol{H}(\boldsymbol{r}) = e^{iM\phi}[H_r(r,z), iH_\phi(r,z), H_z(r,z)]^T \tag{5}$$

where M is the azimuthal mode order.

C. Performance criteria

In our analysis, the performance criteria in designing WG ring resonator are the Q factor and the mode volume. In calculating the Q factor, we consider only the radiation loss for which, Q_{rad} is calculated as follows [5], [8]:

$$Q_{\text{rad}} = \frac{\text{Re}(f)}{2\text{Im}(f)} \tag{6}$$

where $\text{Re}(\cdot)$ and $\text{Im}(\cdot)$ represent respectively the real and imaginary parts of the variable. In the analysis for the domain surrounded by the PLM domain, the real part of the frequency represents the total energy of the domain, whereas the imaginary part represents the rate of energy absorption by the PLM domain, *i.e.* the radiation loss (Chapter 5 in [20]).

In addition, the mode volume is formulated as follows [5], [8]:

$$V_{\text{mode}} = \frac{\int_\Omega \epsilon|\boldsymbol{E}|^2 dx}{\max(\epsilon|\boldsymbol{E}|^2)} \tag{7}$$

where Ω denotes the analysis domain and $\boldsymbol{E}$ is the electric field vector calculated from the Maxwell-Ampère equation without the current density term as follows:

$$\nabla \times \boldsymbol{H} = \epsilon\frac{\partial \boldsymbol{E}}{\partial t} \tag{8}$$

D. Topology optimization

Topology optimization is performed based on density or SIMP interpolation schemes; here SIMP stands for solid isotropic material with penalization [9]. The relative permittivity over the design domain is expressed in terms of a density function $\rho,\ (0 \le \rho \le 1)$:

$$\epsilon = \epsilon_{\text{Air}} + \rho(\epsilon_{\text{GaAlAs}} - \epsilon_{\text{Air}}). \tag{9}$$

The optimal cross-sectional shape of the device can then be specified as a distribution in ρ.

During optimization, we target the following three tasks:

1) Maximization of the Q factor associated with emissions as expressed by equation 6.
2) Minimization of the mode volume as expressed by equation 7.
3) Specification of the emission wavelength $\lambda = c/\text{Re}(f)$,.

Task 3) is first assumed to be satisfied by introducing the corresponding equality constraint. In the eigenfrequency analysis, assuming normalized eigenmodes $\boldsymbol{H}$ ($\int_\Omega |\boldsymbol{H}|^2 dx = 1$), the total electric energy over the analysis domain equals the square of the angular eigenfrequency ($\int_\Omega \epsilon|\boldsymbol{E}|^2 dx = \text{Re}(\omega)^2$) [21], [22]. That is, by pre-specifying emission wavelength and azimuthal mode order, both numerators in the expressions for the Q-factor and mode volume are constant during optimization. Thus, the objective functions for Task 1, J_Q, and Task 2, J_V, and the equality constraint h for Task 3 are formulated as follows:

$$\underset{\rho}{\text{minimize}}\, J_Q(\rho) = \text{Im}(f) \tag{10}$$

or

$$\underset{\rho}{\text{minimize}}\, J_V(\rho) = -\max(\epsilon|\boldsymbol{E}|^2) \tag{11}$$

subject to

$$h(\rho) = \lambda - \lambda_0 = 0 \tag{12}$$

with λ_0 denoting the specified wavelength.

E. Numerical implementation and algorithm

We solve the eigenvalue problem in equation 2 by FEM. To perform the iterating numerical optimization based on the FEM result, the target WG eigenmode is required to be automatically selected from the numerous resulting eigenmodes. The two-step analysis proposed in [6] is introduced to specify the target mode during the optimization iteration. First, we solve the small closed finite-element model composed of the device surrounded by a perfect magnetic wall, as drawn in Fig. 2(a), to obtain the eigenfrequency of the target WG mode. The first eigenmode of the model corresponds to the target WG mode. Second, we solve for the original model surrounded by PLM domains, as drawn in Fig. 2(b), specifying the target eigenfrequency obtained by the closed model.

Since the density function is updated by gradient-based algorithms, sensitivities for both objective function and constraint must be calculated. The sensitivity of the objective function in equation (10) and the equality constraint in equation (12) can be calculated from only state variables without solving the adjoint equation because the optimization problem of the eigenfrequency is self-adjoint [23]. The sensitivity of the objective function in equation (11) is expressible in terms of the functions of the state variable and its adjoint; the adjoint equation is as formulated in [24].

Fig. 3 shows a flowchart of the optimization procedure. First, the closed model is solved by FEM to find the eigenfrequency of the target WG mode. Second, the original open model is solved by FEM and the objective function and the constraint are calculated. Sensitivities for both objective function and constraint must be calculated. Next, the adjoint equation is solved by FEM and the sensitivities of the objective function and the constraint calculated. Finally, the design variables are updated in the first stage of the optimization by the SLP algorithm [25] as it is one of the more basic methods that can handle equality constraints directly. However, topology optimizations sometimes encounter issues related to the gray unclear domain. These domains are hard to identify as belonging to the optimal shape or the void. To prevent such domains from occurring and to obtain a clear non-gray shape, the density function is updated in the latter stage by the phase field method [16] which is a boundary variation methodology based on the density function. Note that the equality constraint can be directly handled by SLP, whereas it is handled indirectly in the phase field method by using an augmented Lagrangian method [25]. These procedures are repeated until the iteration limit is reached or certain convergence criteria hold.

III. Numerical examples

To confirm the validity of the proposed methodology, some numerical examples are studied. The detail of the computational model is first explained. Optimizations are performed

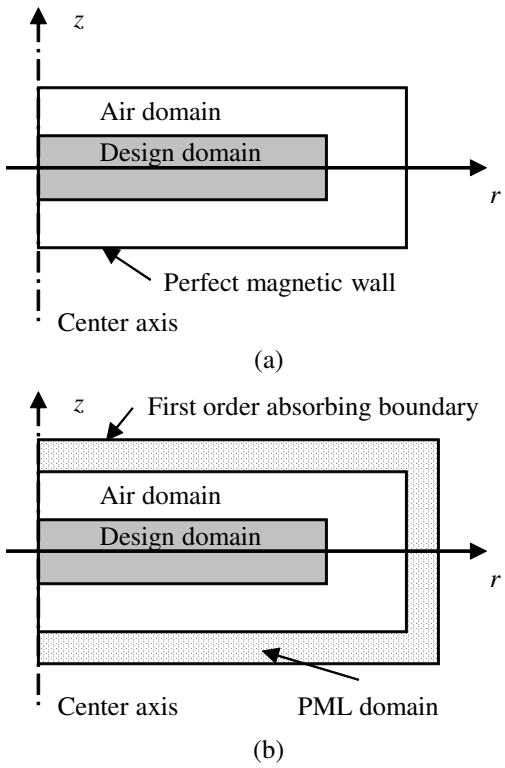

Fig. 2. The analysis domains used in FEM. (a) Closed model. (b) Open model.

with specified TE modes ($p = 1,\ M = 10$, 11 or 12). The size of each is as follows: the air domains of both closed and open models are 1.8 μm $\times$ 3 μm and 4 μm $\times$ 6 μm respectively; the design domain which is identical in both models is 1.5 μm $\times$ 2 μm. The PLM domains are set for the upper, lower and right-side of the open model and their thickness are all 0.25 μm. The design domain is meshed by 75 $\times$ 100 square elements. The other domains are meshed by triangular elements. Using the second-order Lagrange elements for the formulation of each element, the total degrees of freedoms are 105885 and 137052 in the closed model and the open model respectively. The design variable is discretized as a piecewise-constant function on the square finite elements of the design domain. Assuming horizontal mirror symmetry of the optimal shapes, only the upper half of the design domain is optimized. Thus, the 7500 design variables are updated during optimization in this problem. The media constituting the resonator and surrounding domain are assumed to be respectively isotropic GaAlAs with $\epsilon = 11.2896$ and air with $\epsilon = 1$. All FEMs are performed using a commercial software, COMSOL Multiphysics.

A. Optimization for high Q factor

The first optimization is performed with the specified wavelength $\lambda_0 = 1200$nm and azimuthal mode order $M = 11$ targeting to improve the Q factor using the objective function in equation 10. Fig. 4 shows the optimal configuration, the distribution of the electric energy density $\epsilon|E|^2$ and the electric field intensity $|E|^2$. These figures are shown in 1.5 μm

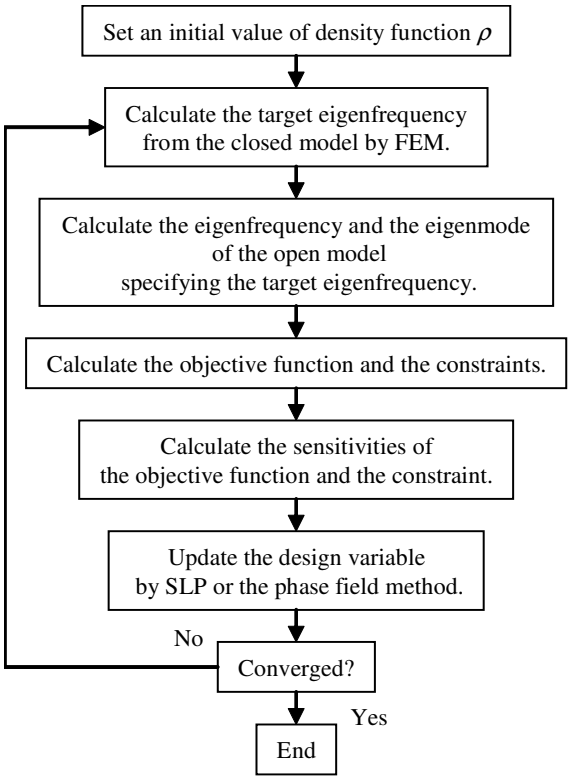

Fig. 3. Flowchart of the optimization procedure

$\times$ 2 μm boxes for which the left side corresponds to the center axis. The resulting Q factor and mode volume are $Q_{\text{rad}} = 5.809 \times 10^7$, $V_{\text{mode}} = 1.716 \times 10^{-19}$. The optimal shape has a large smooth convex form covering the electric-field hot spot to reduce radiation losses.

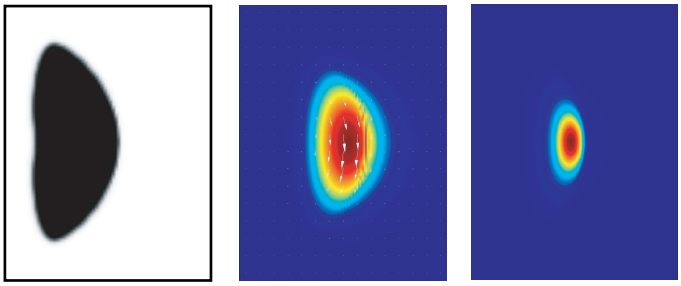

Fig. 4. Optimal result obtained by maximization of Q_{rad} with $\lambda_0 = 1200$nm and $M = 11$. (a) Optimal shape. (b) Electric field intensity $|E|^2$ distribution, with the white arrows indicating the electric field's magnitude and direction in the medial plane. (c) Electric energy density $\epsilon|E|^2$ distribution.

Next, the optimizations of the Q factor are performed for different settings of M and λ_0. Fig. 5 shows the optimal configuration obtained by $(\lambda_0[\text{nm}], M) = (1100, 11), (1300, 11), (1200, 10), (1200, 12)$. Table I shows the comparison of the Q factors and the mode volumes of these optimal shapes. Fig. 5 (b) has larger shapes than (a) to get larger-wavelength light with the same azimuthal mode order. The shapes (c) and (d) have the same characteristics. However, according to Table I, smaller wavelength and larger azimuthal mode order correspond to larger Q_{rad}. Since both conditions lead to increases in wavenumber in the emission mode, in terms of the mode volume, larger shapes have larger values.

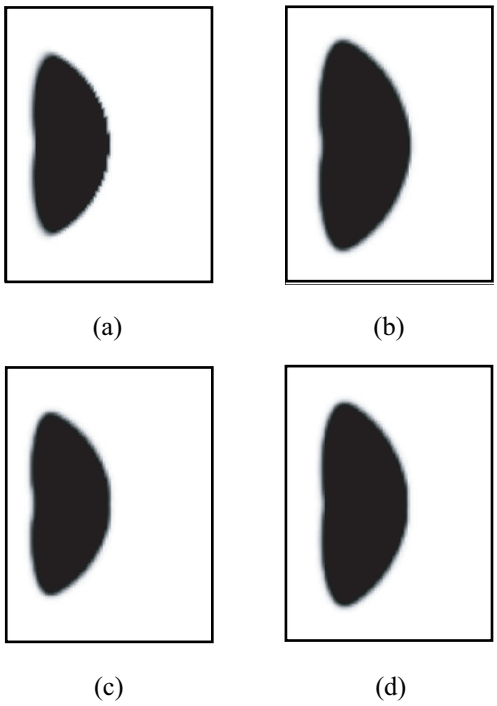

Fig. 5. Optimal shapes obtained by maximization of Q_{rad} with (a) $(\lambda_0[\text{nm}], M) = (1100, 11)$, (b) $(\lambda_0[\text{nm}], M) = (1300, 11)$, (c) $(\lambda_0[\text{nm}], M) = (1200, 10)$ and (d) $(\lambda_0[\text{nm}], M) = (1200, 13)$

B. Optimization for both high Q factor and low mode volume

The optimizations are performed with the view to increasing Q factor and decreasing mode volume as far as possible. The following objective function is introduced by integrating equations 10 and 11 using weighting factor w:

$$\underset{\rho}{\text{minimize}}\, J(\rho) = w * \text{Im}(f) - (1 - w) * \max(\epsilon|\boldsymbol{E}|^2) \quad (13)$$

Varying the weighting coefficient from 0 to 1, six optimal results are encountered; see Fig. 6. Result (a) corresponds to that shown in Fig. 4. As a trade-off exists between Q-factor and mode volume, the set of optimal solutions forms a Pareto-optimal set [17]; better Q_{rad} values must lead to worse V_{mode} and vice versa given the same wavelength and the azimuthal mode order. Fig. 7 shows the electric field intensity corresponding to shape (f). In contrast to high Q factor shape, the low-mode-volume optimal shape has a small concave form near the center to enhance the maximum electric energy. The interpolated shapes (b)-(e) have both characteristics. The concentrations of the electric field and the electric energy at the center of the device are observed in shape (f) whereas shape (a) has a wider hot spot. Moreover, to maintain the emission wavelength for the same azimuthal mode order but different shapes, the location of the cross-section moves off-center as the cross-sectional area becomes smaller. With normalization of the eigenmode, the square of the emission frequency equals

TABLE I
COMPARISON OF Q_{RAD} AND V_{MODE} AMONG OPTIMAL RESULTS

$(\lambda_0[nm], M)$	(1200,11)	(1100,11)	(1300,11)	(1200,10)	(1200,12)
Q_{rad}	5.809×10^7	5.943×10^7	5.660×10^7	1.018×10^7	3.303×10^8
V_{mode}	1.716×10^{-19}	1.342×10^{-19}	2.224×10^{-19}	1.526×10^{-19}	1.989×10^{-19}

the total electric energy of the resonator and fixed. Thus, the total energy of the cross-section, which relates the area and the diameter at the center of the cross-section, are inversely related.

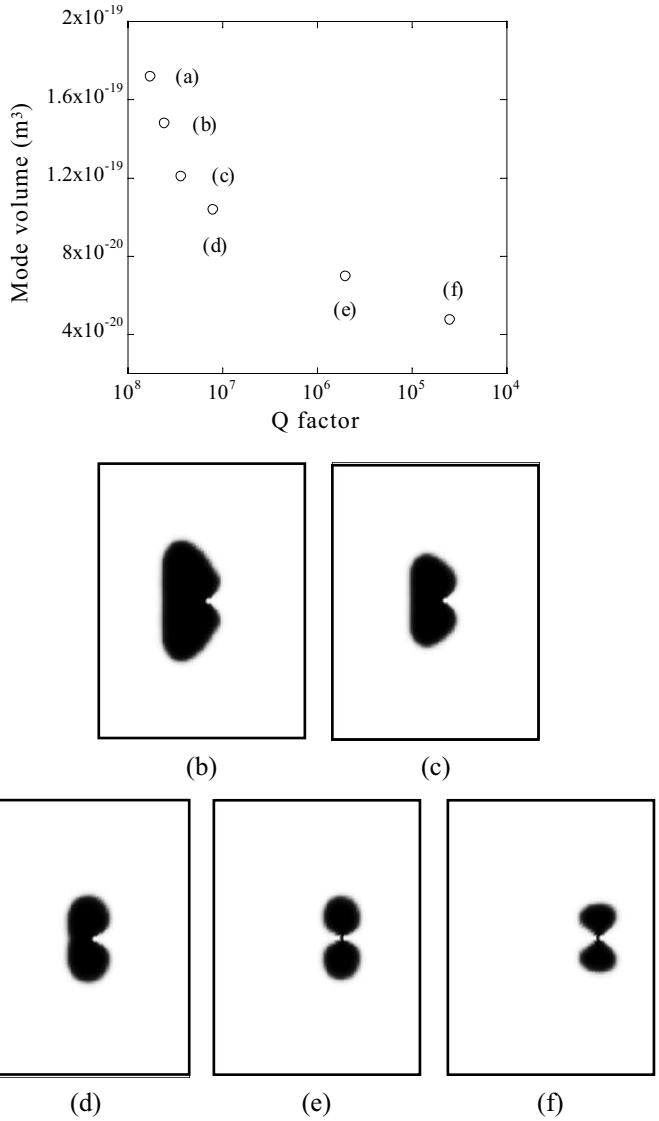

Fig. 6. Optimal shapes and their performances, obtained by maximizing Q_{rad} and minimizing V_{mode} with different weighting factor settings in equation (13).

C. Comparison with existing shapes

Our optimal results are compared with existing shapes. Since the stays were eliminated during optimizations, shapes shown in Fig. 6 have no support structure connecting the center and the main cross-section. To make practical structures, 0.16 μm stays were added to shapes (a) and (b), specifically, 0.08 μm stays to (c) and (d), and 0.04 μm stays to shapes (e) and (f). In shapes (e) and (f), stays significantly affected the performance index and the emission wavelength. Thus, re-optimizations were performed for these two shapes. The results are shown in Fig. 9 with each shape finally having almost the same performance and mode shape as the corresponding shape shown in 6. These are all compared with the two existing shapes, the disc having trapezoidal cross-section studied in [8] and the toroid having circular cross-section studied in [7]. A parametric study was performed varying the radius r and thickness t in the disc device and the radius r and diameter of the side circle d in the toroidal device, both of which are schematically drawn in Fig. 8. The ranges and step sizes of these parameters are shown in Table II. Both Q factor and mode volumes are calculated for all cross-sectional shapes and those results having a 1200[nm] emission wavelength identified. Some of the more striking results are plotted in Fig. 9. The optimal solution obtained by the proposed methodology achieved a better performance in both high Q factor and low-mode volume ranges, since existing shapes do not have either a semicircular shape for high Q factor or concave shape for low mode volume.

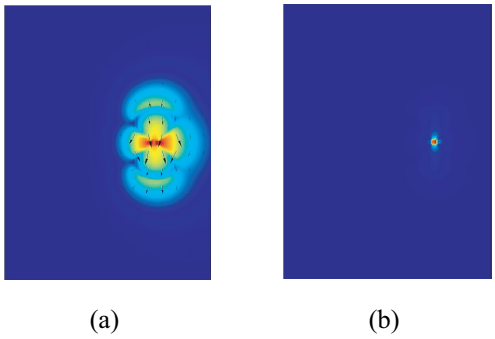

Fig. 7. (a) Electric field intensity $|E|^2$ distribution with black arrows indicating the electric field's magnitude and direction in the medial plane and (b) Electric energy density $\epsilon|E|^2$ distribution of optimal result shown in Fig. 6(f)

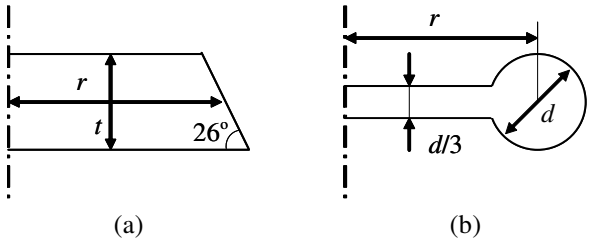

Fig. 8. Settings of design parameters in existing shapes used in the comparison with optimal shapes. (a) Disk shape. (b) Toroidal shape.

TABLE III
COMPARISON OF THE PURCELL FACTOR AMONG OPTIMAL RESULTS AND EXISTING SHAPES.

	Optimal shape in Fig. 10	Optimal shapes in Fig. 9 (a)	(b)	(c)	(d)	(e)	(f)	Disc	Toroidal
$F_P(\times 10^{-3})$	1.210	1.171	0.997	0.821	0.489	2.335×10^{-2}	2.247×10^{-2}	0.657	0.335

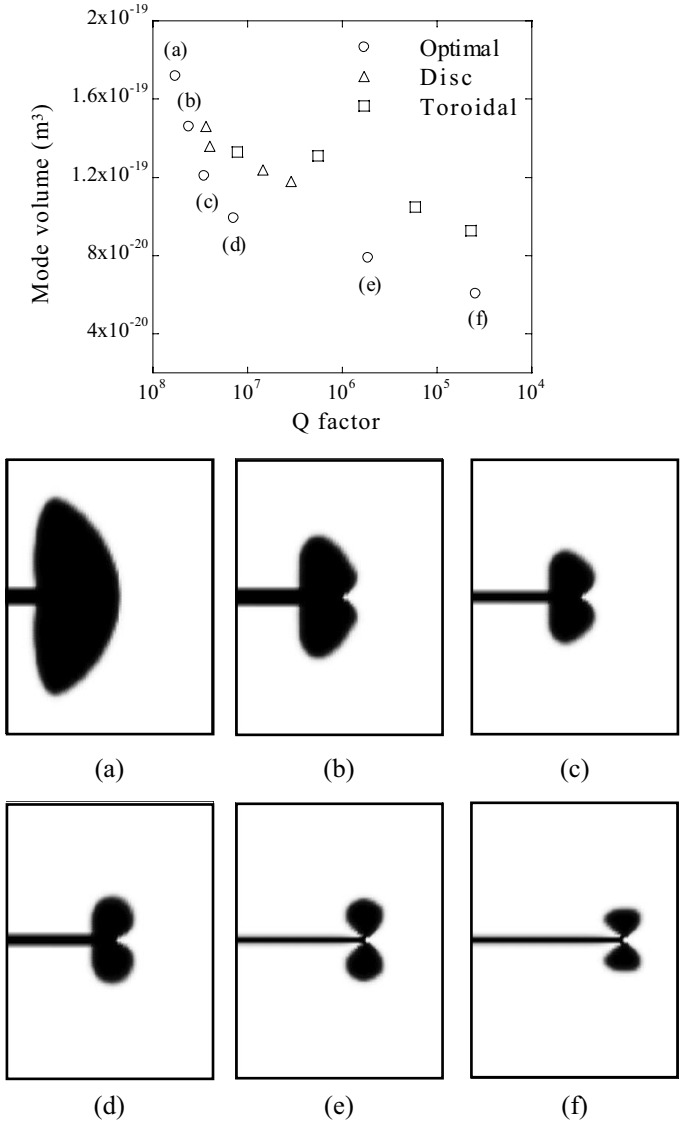

Fig. 9. Optimal shapes with stays obtained by maximizing Q_{rad} and minimizing V_{mode} and their performances in comparison with existing shapes.

D. Optimization of the Purcell factor

In real applications, such as micro laser resonators, the Q factor and the mode volume are not treated independently. The Purcell factor [18] is an integrated index that dictates spontaneous emission rates in devices:

$$F_P = \frac{3}{4\pi^2}\left(\frac{\lambda}{n}\right)^3\left(\frac{Q}{V_{\text{mode}}}\right) \tag{14}$$

where n is the refractive index of the device material. For example, F_P maximization leads to low threshold lasers. Since the emission wavelength is specified by the equality constraint

TABLE II
PARAMETER SETTINGS FOR EXISTING SHAPES SHOWN IN FIG. 8

Type	Parameter	Interval	Step size
Disk	r[m]	$7.5 \times 10^{-7} \le r \le 1.15 \times 10^{-6}$	5×10^{-8}
	t[m]	$2 \times 10^{-7} \le t \le 1.5 \times 10^{-6}$	2×10^{-8}
Toroidal	r[m]	$7.5 \times 10^{-7} \le r \le 1.25 \times 10^{-6}$	5×10^{-8}
	d[m]	$2 \times 10^{-7} \le d \le 1.5 \times 10^{-6}$	2×10^{-8}

in the proposed methodology, maximization via equation 14 can be reduced to maximization of the ratio between Q and V_{mode}. Thus, in combining equations 10 and 11, we use the following objective function:

$$\underset{\rho}{\text{minimize}}\ \frac{J_Q}{J_V} = -\frac{\max(\epsilon|\boldsymbol{E}|^2)}{\text{Im}(f)}. \tag{15}$$

The optimal configuration is shown in Fig. 10. Table III shows a comparison of the Purcell factor for the result with the previous optimal results. From the results for disk- and toroidal-type devices shown in Fig. 9, the optimal choices of shape are those with $t = 7.5 \times 10^{-7}$, $t = 1.02 \times 10^{-6}$ and $t = 7.5 \times 10^{-7}$, $t = 4 \times 10^{-7}$. Since the shape shown in Fig. 10 was best of all, the validity of the proposed objective function is confirmed. However, the difference between the results for the shapes given in Fig. 10 and Fig. 9(a) is slight, indicating that the effect of the term pertaining to Q factor is much larger than the one pertaining to mode volume in equation 15. Table III also indicates a higher Q factor leads to a higher value of Purcell factor. Thus, considering the Q factor could be enough to maximize the Purcell factor under the condition that the emission wavelength and the azimuthal mode order are both specified.

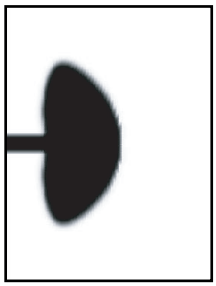

Fig. 10. Optimal shape obtained by maximizing Purcell factor.

IV. CONCLUSION

In this research, we studied and identified optimal shapes for WG micro-ring resonators having high Q factor and low mode volume. The systematic procedure helps to find optimal device shapes with certain designed performance given prescribed

emission wavelength and WG resonance mode. As a basic principle for designing WG micro-ring resonators, we found that large convex shapes produced high Q factors; small concave shapes produced low mode volumes. By comparing these optimal shapes obtained numerically with existing shapes, better performances were clearly observed. Moreover, we performed an optimization of the Purcell factor, which has practical relevance in design that includes Q factor and mode volume. However, maximization of Q factor alone yields an almost identical result indicating that Q-factor maximization results in the maximization of the Purcell factor given emission wavelength and WG resonance mode.

Manufacturing conditions were ignored in this study. Because of the nature of etching processes and surface tensions used to make micro-resonators, experimental micro-resonators must have sharp edges. In particular, deep cusps such exhibited in the low mode volume shape are hard to manufacture. Thus, the shapes found in this study will be difficult to investigate experimentally. However, the fundamental finding we obtained from optimization will enable better practical design shapes.

ACKNOWLEDGMENT

We would like to thank the anonymous reviewer of an early version of this paper for valuable and helpful comments.

REFERENCES

[1] S. McCall, A. Levi, R. Slusher, S. Pearton, and R. Logan, "Whispering-gallery mode microdisk lasers," *Appl. Phys. Lett.*, vol. 60, no. 3, pp. 289–291, 1992.

[2] K. J. Vahala, "Optical microcavities," *Nature*, vol. 424, pp. 839–846, 2003.

[3] A. B. Matsko and V. S. Ilchenko, "Optical resonators with whispering-gallery modes-part i: basics," *IEEE J. Sel. Top. Quant. Electron.*, vol. 12, no. 1, pp. 3–14, 2006.

[4] V. S. Ilchenko and A. B. Matsko, "Optical resonators with whispering-gallery modes-part ii: applications," *IEEE J. Sel. Top. Quant. Electron.*, vol. 12, no. 1, pp. 15–32, 2006.

[5] A. Oraevsky, "Whispering-gallery waves," *Quant. Electron.*, vol. 32, no. 5, pp. 377–400, 2002.

[6] M. Oxborrow, "Traceable 2-d finite-element simulation of the whispering-gallery modes of axisymmetric electromagnetic resonators," *IEEE Trans. Microw. Theor. Tech.*, vol. 55, no. 6, pp. 1209–1218, 2007.

[7] S. M. Spillane, T. J. Kippenberg, K. J. Vahala, K. W. Goh, E. Wilcut, and H. J. Kimble, "Ultrahigh-q toroidal microresonators for cavity quantum electrodynamics," *Phys. Rev.*, vol. 71, no. 1, p. 013817, 2005.

[8] K. Srinivasan, M. Borselli, O. Painter, A. Stintz, and S. Krishna, "Cavity q, mode volume, and lasing threshold in small diameter algaas microdisks with embedded quantum dots," *Optic. Express*, vol. 14, no. 3, pp. 1094–1105, 2006.

[9] M. P. Bendsøe and O. Sigmund, *Topology Optimization: Theory, Methods, and Applications*. Berlin: Springer-Verlag, 2003.

[10] J. Jensen and O. Sigmund, "Systematic design of photonic crystal structures using topology optimization: Low-loss waveguide bends," *Appl. Phys. Lett.*, vol. 84, no. 12, pp. 2022–2024, 2004.

[11] W. R. Frei, D. A. Tortorelli, and H. T. Johnson, "Topology optimization of a photonic crystal waveguide termination to maximize directional emission," *Appl. Phys. Lett.*, vol. 86, p. 111114, 2005.

[12] W. R. Frei, D. A. Tortorelli, and H. T. Johnson, "Geometry projection method for optimizing photonic nanostructures," *Optic. Lett.*, vol. 32, no. 1, pp. 77–79, 2007.

[13] J. Andkjær, S. Nishiwaki, T. Nomura, and O. Sigmund, "Topology optimization of grating couplers for the efficient excitation of surface plasmons," *J. Opt. Soc. Am. B*, vol. 27, no. 9, pp. 1828–1832, 2010.

[14] A. R. Diaz and O. Sigmund, "A topology optimization method for design of negative permeability metamaterials," *Struct. Multidisc. Optim.*, vol. 41, no. 2, pp. 163–177, 2010.

[15] J. Andkjær and O. Sigmund, "Topology optimized low-contrast all-dielectric optical cloak," *Appl. Phys. Lett.*, vol. 98, no. 2, p. 021112, 2011.

[16] A. Takezawa, S. Nishiwaki, and M. Kitamura, "Shape and topology optimization based on the phasefield method and sensitivity analysis," *J. Comput. Phys.*, vol. 229, no. 7, pp. 2697–2718, 2010.

[17] K. Deb, *Multi-Objective Optimization Using Evolutionary Algorithms*. Chichester: Wiley, 2009.

[18] E. M. Purcell, "Spontaneous emittion probabilities at radio frequencies," *Phys. Rev.*, vol. 69, p. 681, 1946.

[19] M. Koshiba, K. Hayata, and M. Suzuki, "Improved finite-element formulation in terms of the magnetic field vector for dielectric waveguides," *IEEE Trans. Microw. Theor. Tech.*, vol. 33, no. 3, pp. 227–233, 1985.

[20] D. W. Prather, S. Shi, A. Sharkawy, J. Murakowski, and G. J. Schneider, *Photonic Crystals, Theory, Applications and Fabrication*. Hoboken: Wiley, 2009.

[21] S. H. Gould, *Variational Methods for Eigenvalue Problems: An Introduction to the Methods of Rayleigh, Ritz, Weinstein, and Aronszajn*. New York: Dover Publications, 1995.

[22] G. Allaire, *Numerical Analysis and Optimization: An Introduction to Mathematical Modelling and Numerical Simulation*. Oxford University Press, 2007.

[23] E. J. Haug, K. K. Choi, and V. Komkov, *Design Sensitivity Analysis of Structural Systems*. Orlando: Academic Press, 1986.

[24] G. Allaire, *Conception Optimale De Structures*. Berlin: Springer-Verlag, 2007.

[25] J. Nocedal and S. Wright, *Numerical Optimization*, 2nd ed. New York: Springer, 2006.